Electronic Supplementary Material (ESI) for Journal of Materials Chemistry A.

Supporting information

for

Nanoporous gold supported chromium-doped NiFe oxyhydroxides as high-performance catalysts for oxygen evolution reaction

Jie-Song Sun, Yi-Tong Zhou, Rui-Qi Yao, Hang Shi, Zi Wen, Xing-You Lang,* and Qing Jiang

Key Laboratory of Automobile Materials (Jilin University), Ministry of Education, and School of Materials Science and Engineering, Jilin University, Changchun 130022, China. E-mail: xylang@jlu.edu.cn

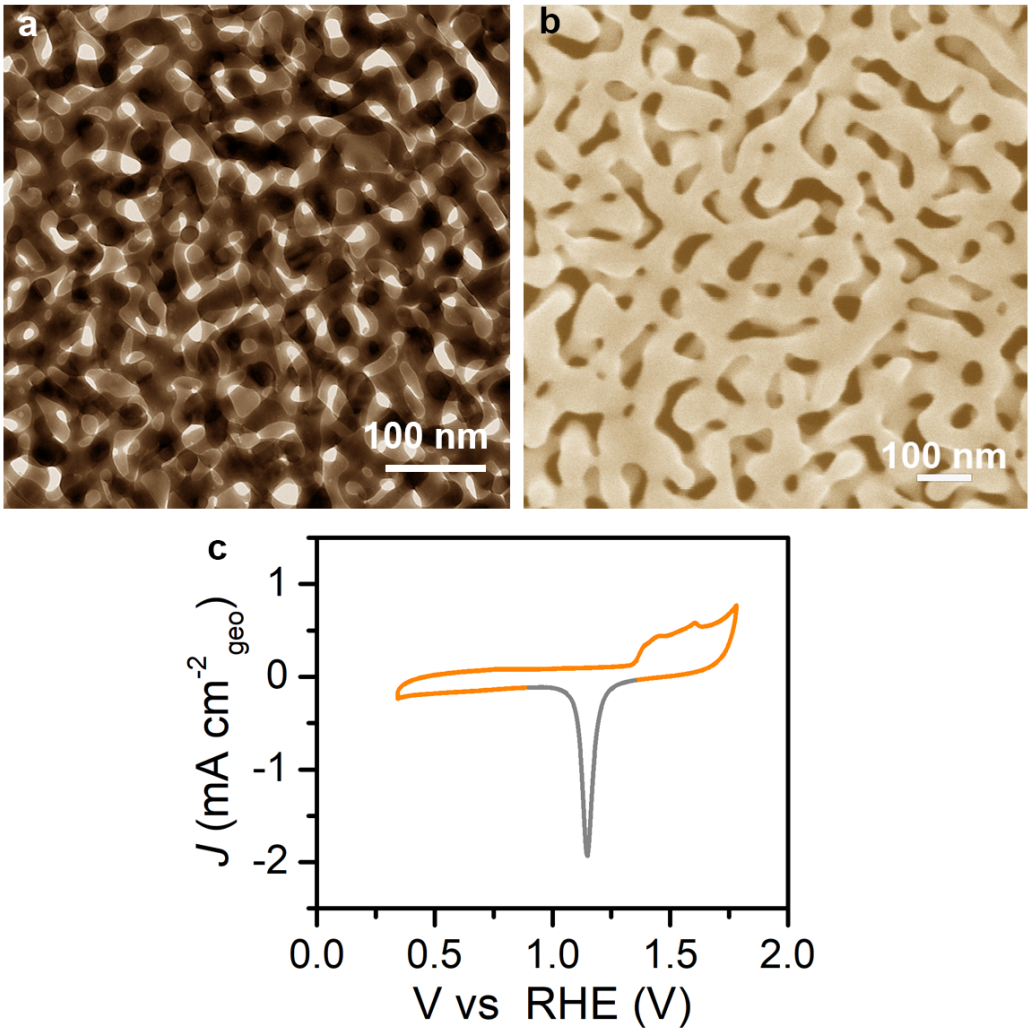

Fig. S1. Typical (a) SEM image and (b) TEM image for bare NP Au film that is prepared by chemically dealloying $Ag_{65}Au_{35}$ films with 100 nm thickness. (c) Typical CV curve of bare NP Au films with a scan rate of 100 mV s^{-1} in 0.5 M H_2SO_4 solution. The ECSA of the NP Au is determined to be 3.0 cm^2 cm^{-2}_{geo} by integrating the charge of Au reduction peak with a conversion factor of 482 μC cm^{-2} for Au.

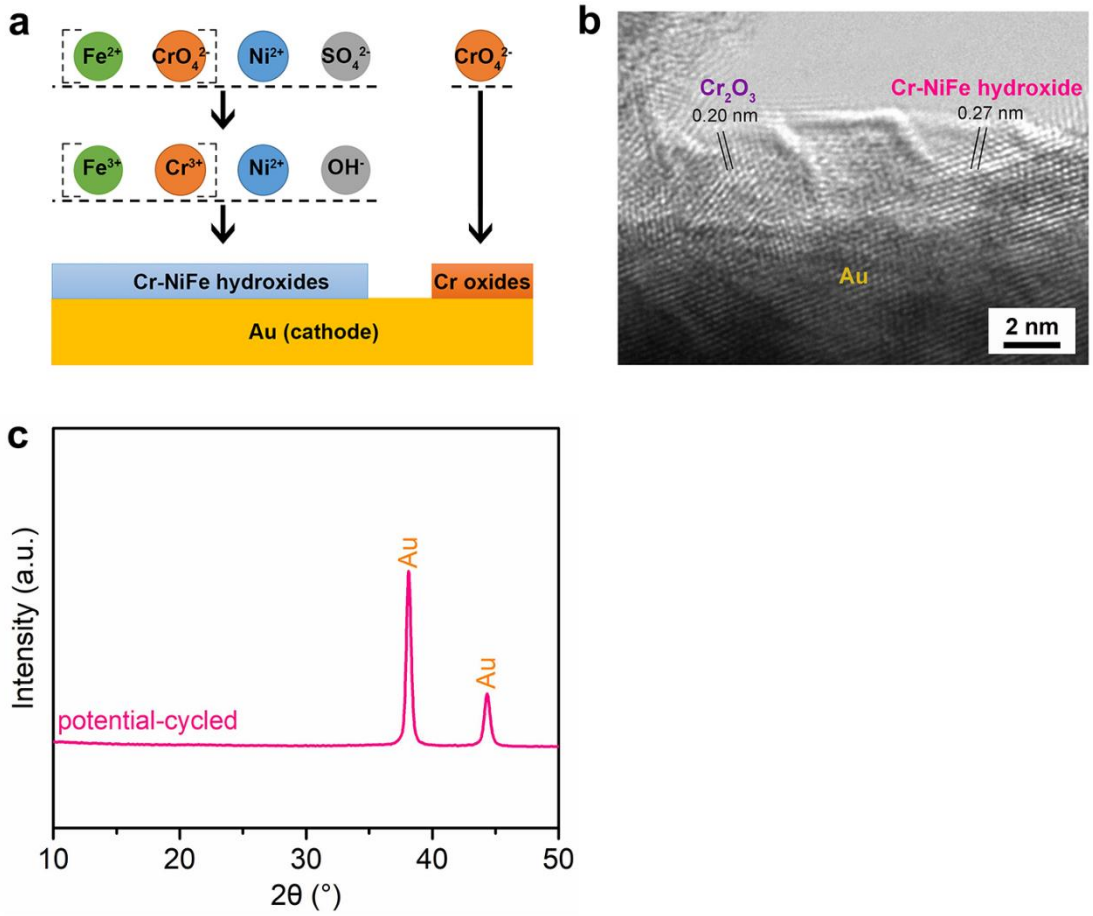

Fig. S2. (a) Schematic diagram for preparing NP Au/Cr-NiFe hybrid electrodes by electrochemical cathode deposition. Using the redox reaction between Fe^{2+} and CrO_4^{2-},[1] it is helpful to dope $[FeO_6]$-$[CrO_6]$ structural units into Ni hydroxides. (b) Typical HRTEM for as-prepared NP Au/Cr-NiFe hybrid electrode with the interplanar spacings of 0.27 nm and 0.20 nm corresponding to (101) lattice planes of Cr-NiFe hydroxide and (202) lattice planes of Cr_2O_3, respectively. (c) Typical XRD patterns for potential-cycled NP Au/Cr-NiFe hybrid electrodes. In addition to characteristic peaks of the Au, the XRD diffraction peaks of the constituent Cr-doped NiFe oxyhydroxide hardly can be detected due to low loading amount.

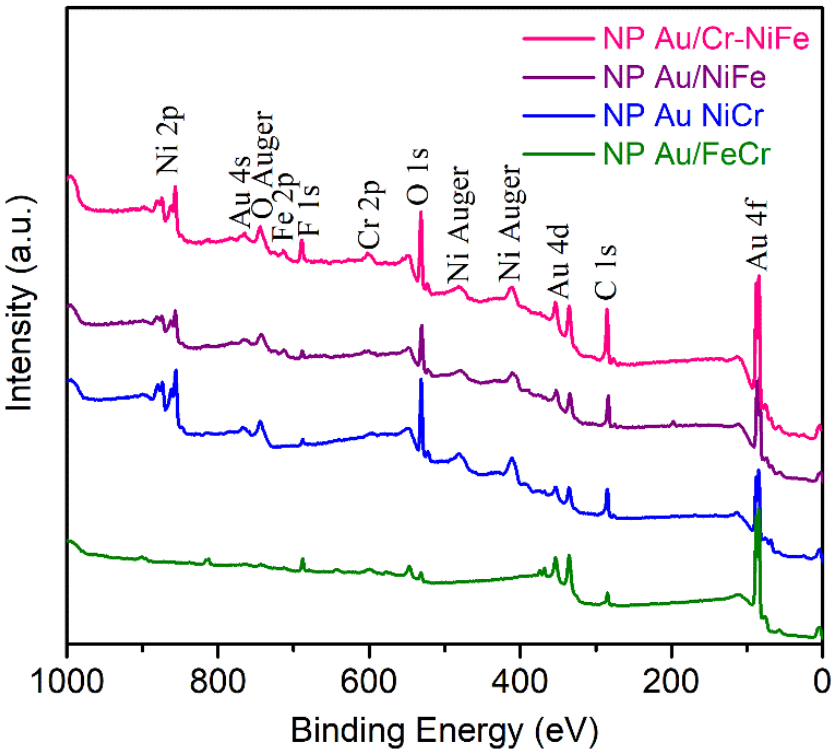

Fig. S3. XPS survey spectrum for potential-cycled NP Au/Cr-NiFe, NP Au/NiFe, NP Au/NiCr and NP Au/FeCr hybrid electrodes.

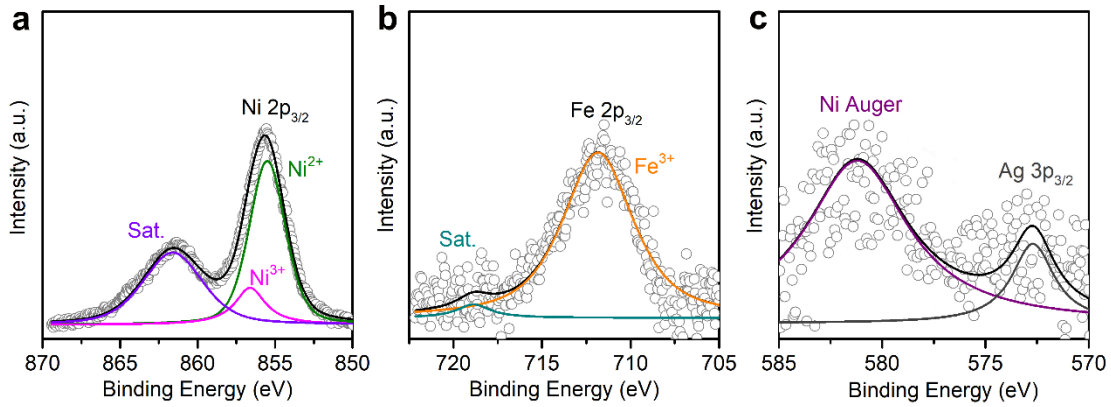

Fig. S4. High-resolution XPS spectra of (a) Ni $2p_{3/2}$, (b) Fe $2p_{3/2}$ and (c) Cr $2p_{3/2}$ for potential-cycled NP Au/NiFe hybrid electrode. The Ag element is the residual component in NP Au film.

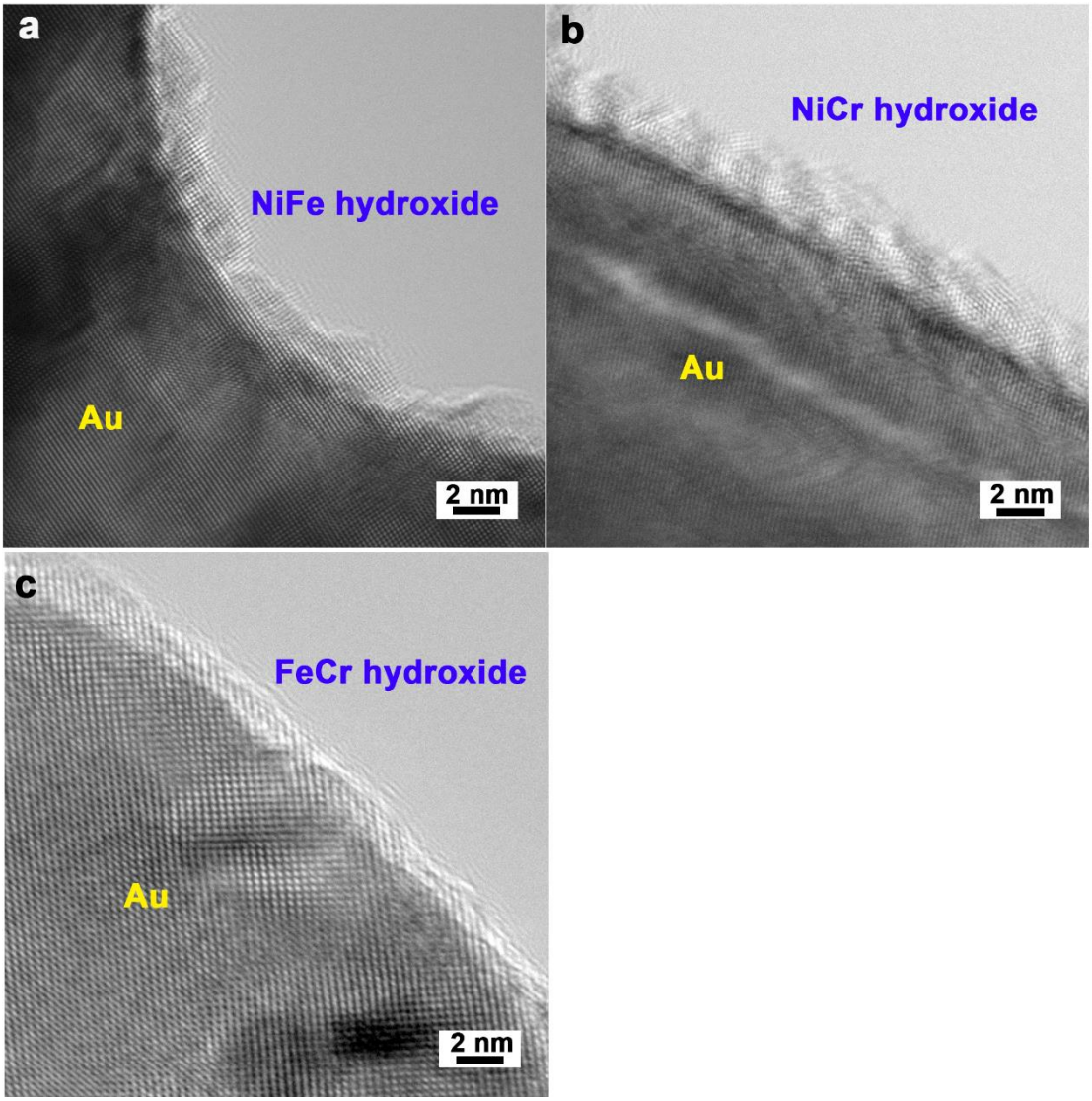

Fig. S5. Typical HRTEM images for (a) NP Au/NiFe, (b) NP Au/NiCr and (c) NP Au/FeCr hybrid electrodes.

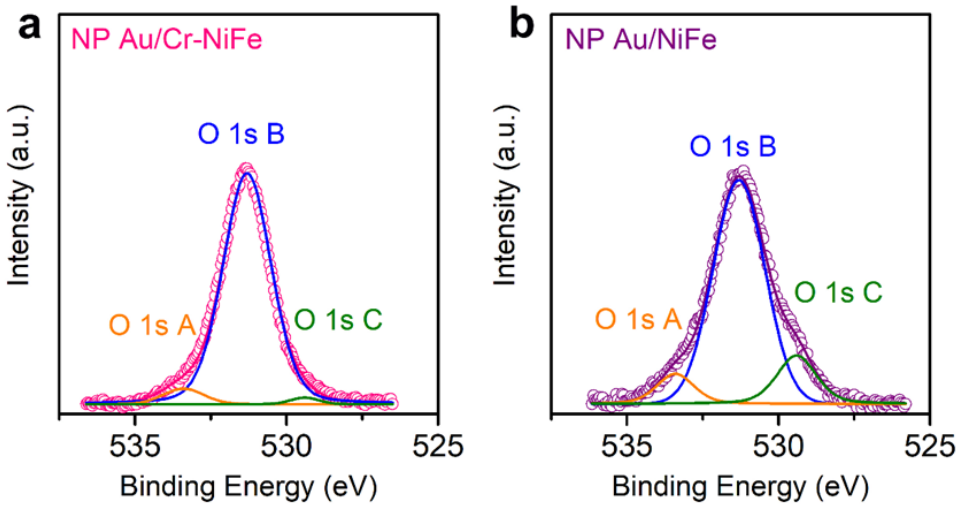

Fig. S6. High-resolution XPS spectra of O 1s for (a) potential-cycled NP Au/Cr-NiFe and (b) potential-cycled NP Au/NiFe, respectively. The O 1s spectra reveals three distinct peaks: O 1s A (533.4 eV) assigned to oxygen species in the surface-adsorbed H_2O molecules, O 1s B (531.3 eV) associated with oxygen from the α-$Ni(OH)_2$ and γ-NiOOH, and O 1s C (529.3 eV) attributed to the binding energies of lattice oxygen in interconnected [FeO_6] octahedrons, which reflects the dispersion degree of Fe atoms in (oxy)hydroxides.

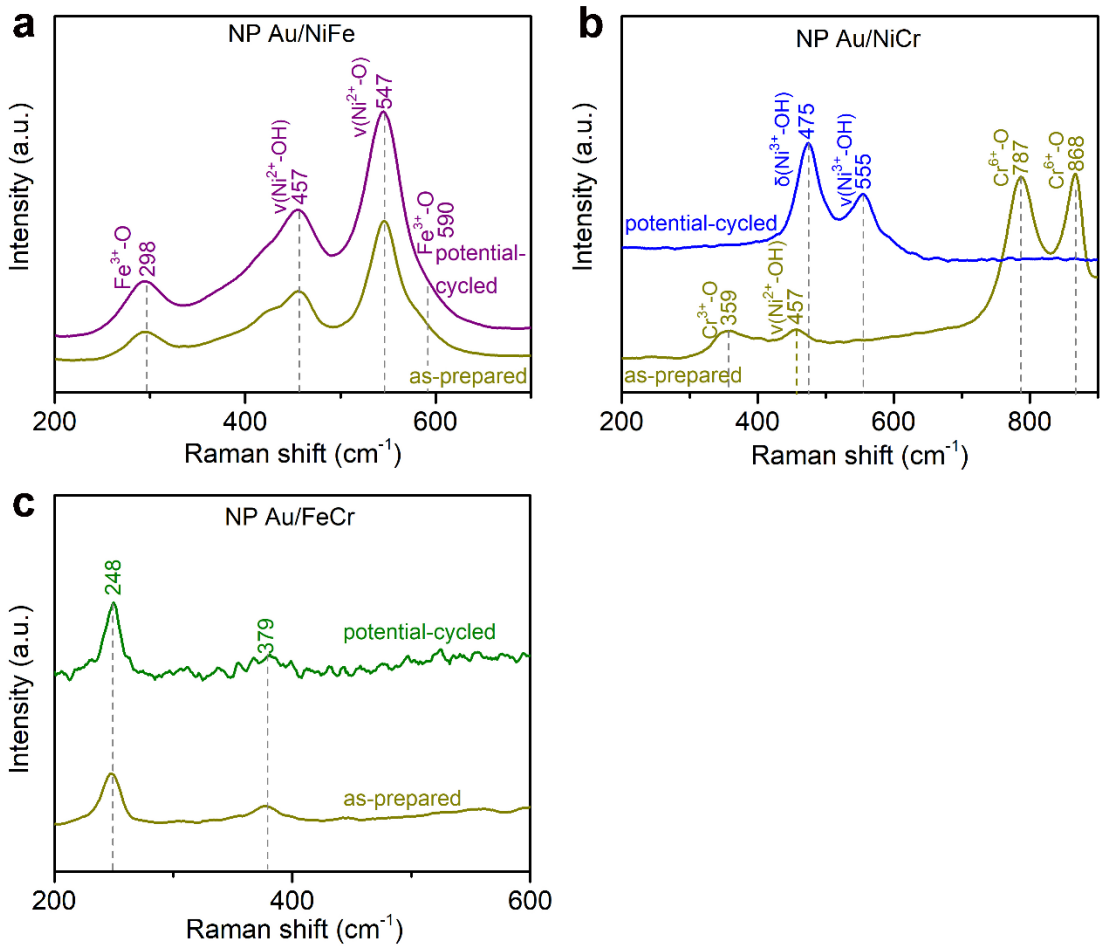

Fig. S7. Typical surface-enhanced Raman spectrum for as-prepared and potential-cycled (a) NP Au/NiFe, (b) NP Au/NiCr and (c) NP Au/FeCr hybrid electrodes. Raman peaks at 248 cm^{-1} and 379 cm^{-1} indicate Cr doped FeOOH with γ phase are deposited on NP Au skeletons.

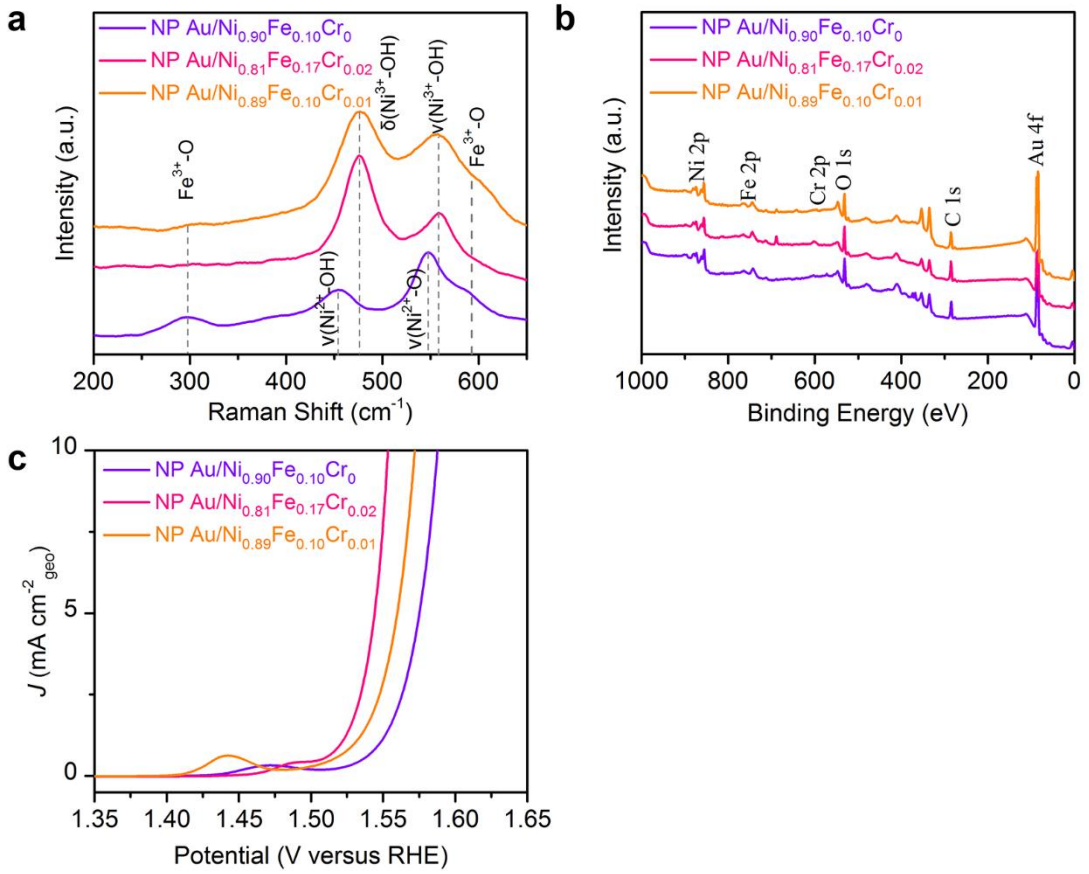

Fig. S8. (a) Raman spectra and (b) XPS survey spectra for potential-cycled NP Au/Cr-NiFe hybrid electrodes with different Ni/Fe/Cr compositions, which are prepared by adjusting the concentrations of CrO_4^{2-} in the initial electroplating solutions. (c) Typical OER polarization curves for potential-cycled NP Au/Cr-NiFe hybrid electrodes with different Ni/Fe/Cr compositions.

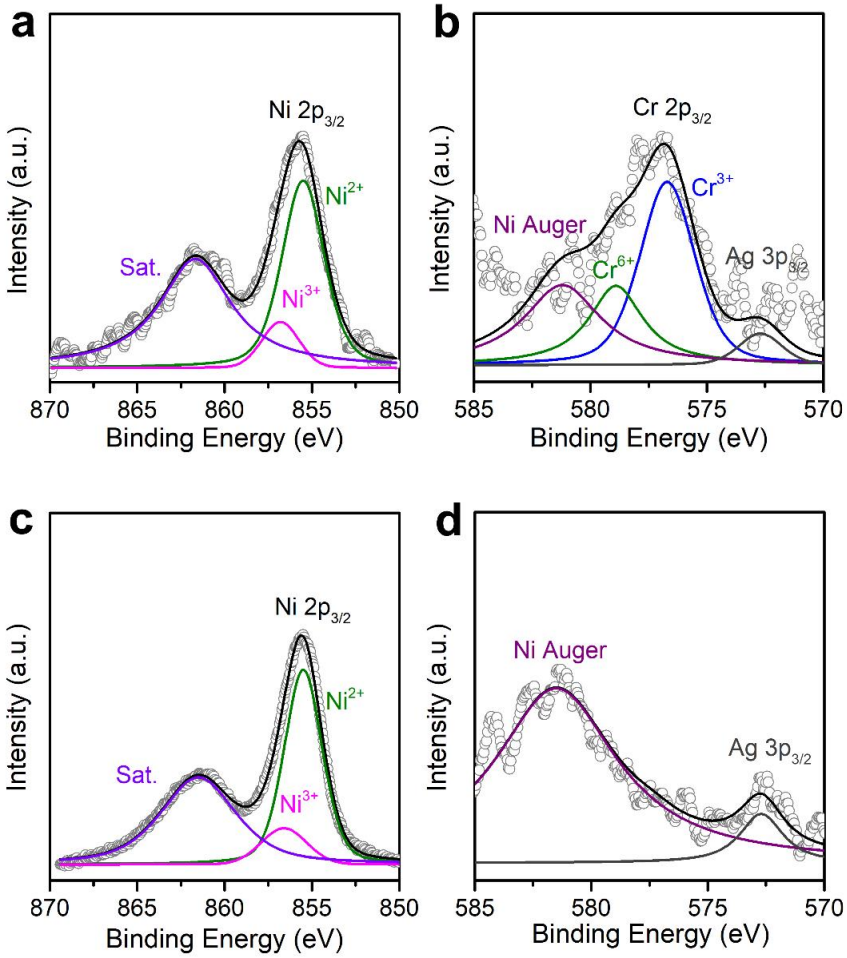

Fig. S9. High-resolution (a) Ni $2p_{3/2}$ and (b) Cr $2p_{3/2}$ XPS spectra for as-deposited NP Au/NiCr hybrid electrode with the Ni/Cr atomic ratio of 85/15. Cr^{3+} (576.7 eV) and Cr^{6+} (578.9 eV) peaks indicate that Cr element exists as Cr oxides in as-deposited NP Au/NiCr hybrid electrode. High-resolution (c) Ni $2p_{3/2}$ and (d) Cr $2p_{3/2}$ XPS spectra for potential-cycled NP Au/NiCr hybrid electrode. Cr $2p_{3/2}$ spectra indicates that Cr oxides in as-deposited NP Au/NiCr are dissolved in 0.1 M KOH solution after testing. The Ag element is the residual component in nanoporous gold films that are fabricated by chemically dealloying Au-Ag alloy films.

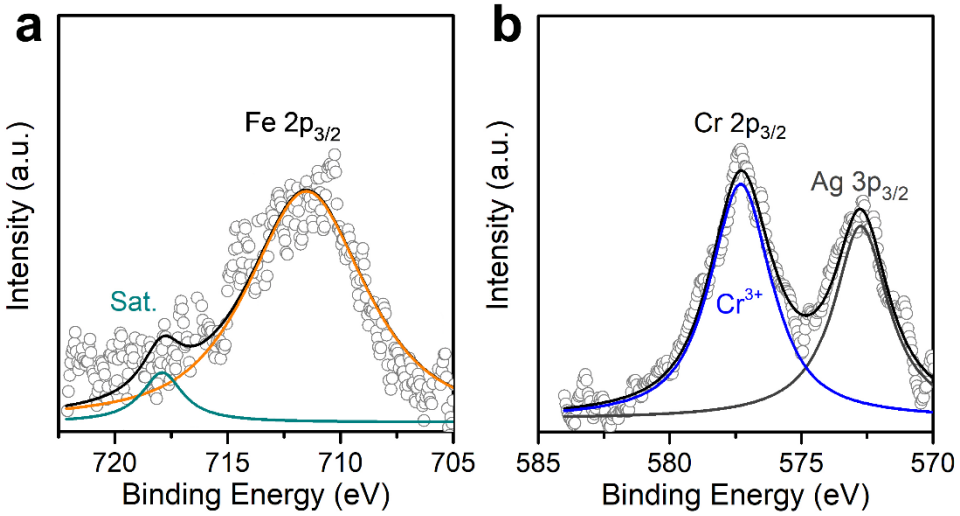

Fig. S10. High-resolution (a) Fe $2p_{3/2}$ and (b) Cr $2p_{3/2}$ XPS spectra for as-deposited NP Au/FeCr hybrid electrode with the Fe/Cr composition of 55/45. The binding energy of Fe $2p_{3/2}$ and Cr $2p_{3/2}$ locate at 711.5 eV and 577.3 eV.

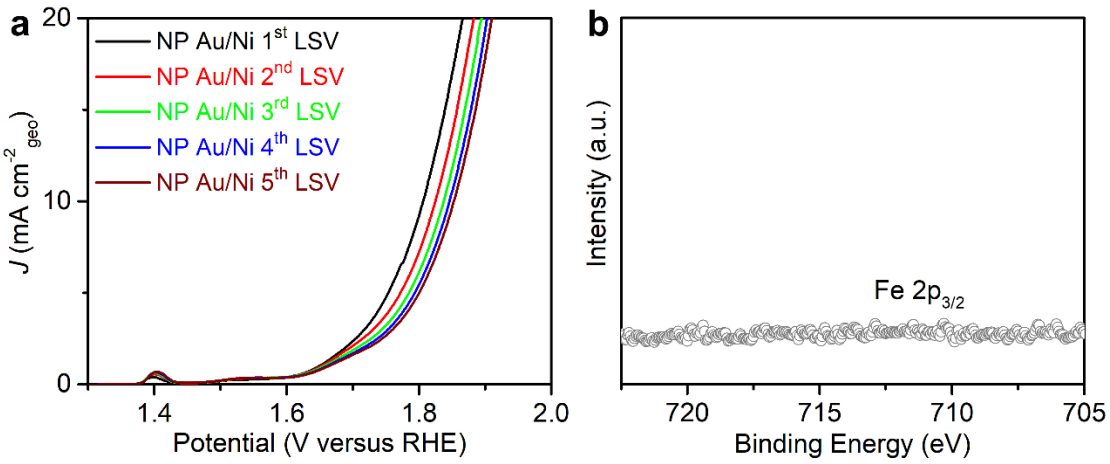

Fig. S11. (a) The first five LSV curves for NP Au/Ni hybrid electrode in purified 0.1 M KOH solution. With the increase of the cycle number, the more NiOOH can fully contact with the electrolyte, thus showing the larger oxidation peak. However, there is a slight reduction in OER current density, which is consistent with previous reports.[1] (b) High-resolution XPS spectra of Fe $2p_{3/2}$ for potential-cycled NP Au/Ni hybrid electrode. No Fe impurities from the electrolyte is found to be adsorbed on the potential-cycled NP Au/Ni hybrid electrode, which indicates that the purified 0.1 M KOH solution does not interfere with the OER intrinsic activity of hybrid electrodes.

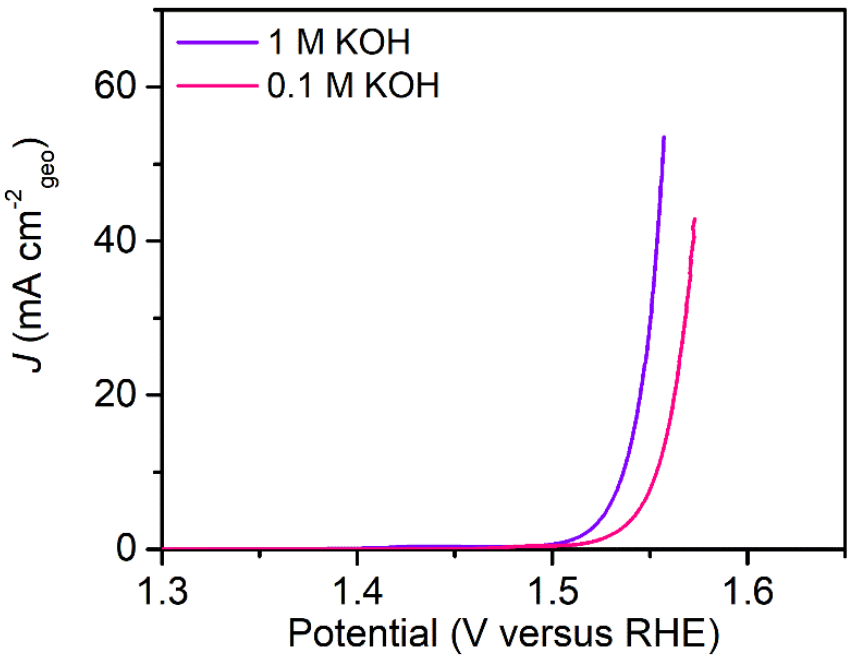

Fig. S12. Typical LSV curves for the NP Au/Cr-NiFe hybrid electrode in 0.1 M KOH and 1 M KOH solutions.

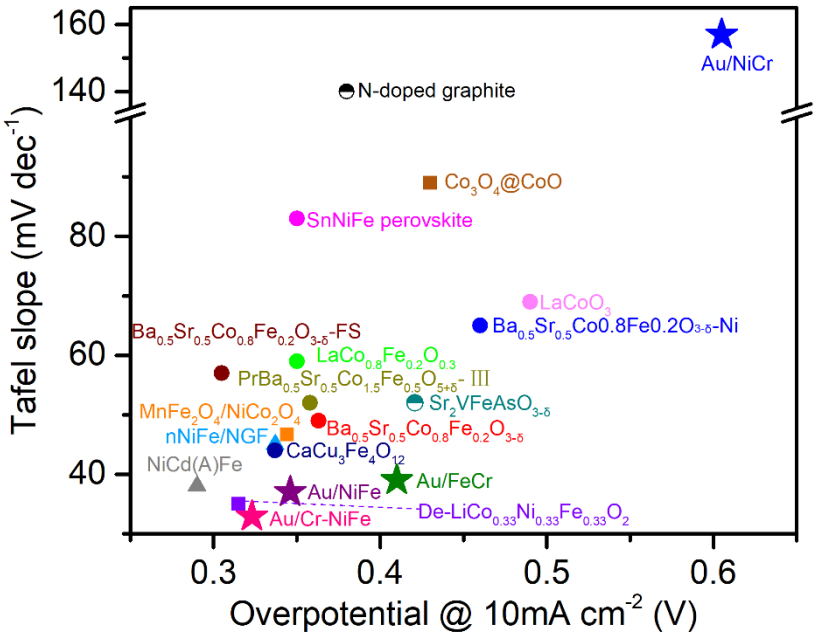

Fig. S13. The Tafel slope and the overpotential of NP Au/Cr-NiFe hybrid electrode at 10 mA cm^{-2}_{geo} in 0.1 M KOH solution, comparing with representative OER catalysts, such as N-doped graphite,[2] Co_3O_4@CoO,[3] SnNiFe perovskite,[4] $Ba_{0.5}Sr_{0.5}Co_{0.8}Fe_{0.2}O_{3-\delta}$-Ni,[5] $LaCo_{0.8}Fe_{0.2}O_3$,[6] $CaCu_3Fe_4O_{12}$ [7] and De-$LiCo_{0.33}Ni_{0.33}Fe_{0.33}O_2$.[8]

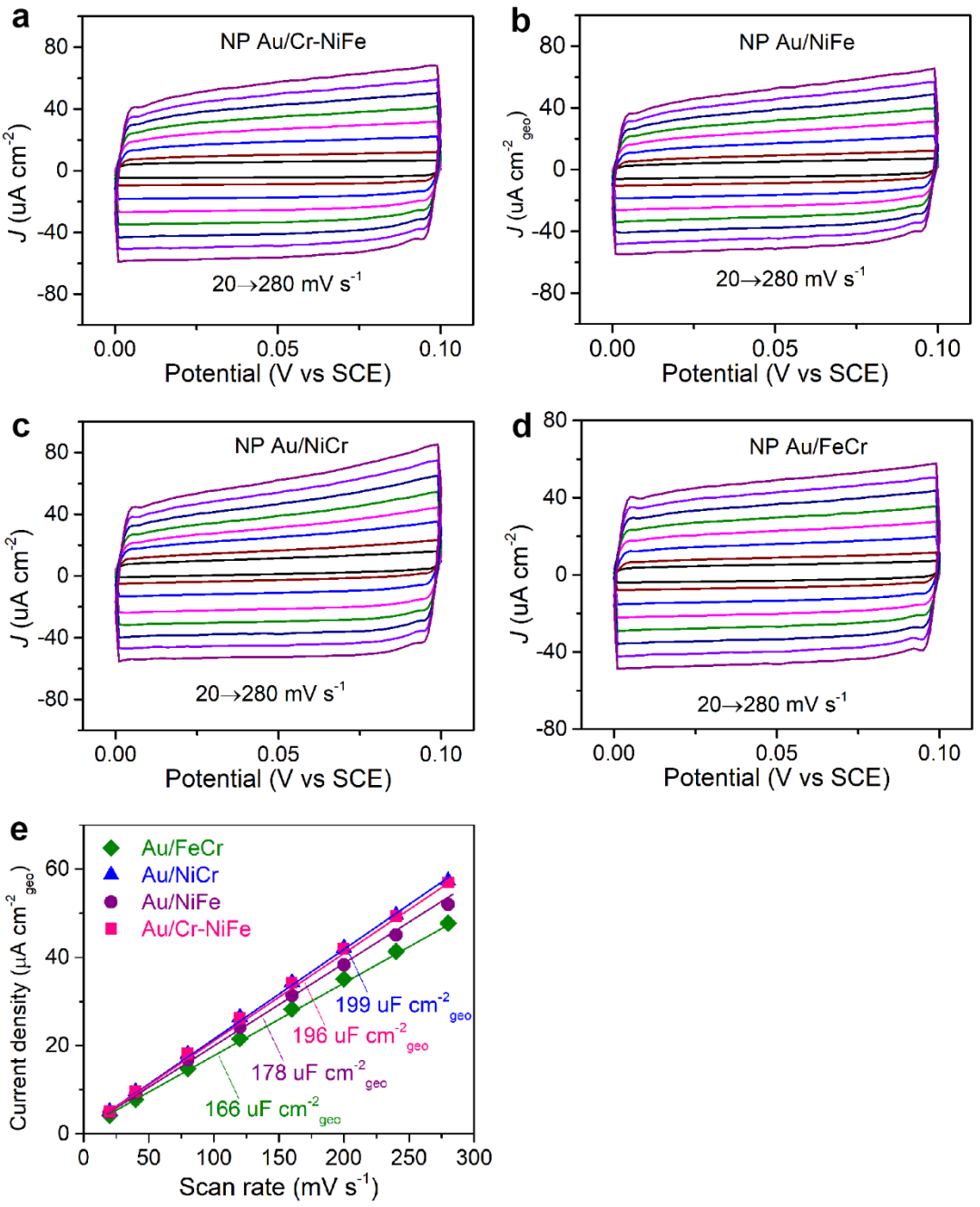

Fig. S14. Typical CV curves for (a) NP Au/Cr-NiFe, (b) NP Au/NiFe, (c) NP Au/NiCr and (d) NP Au/FeCr hybrid electrodes at the scan rates from 20 to 280 mV s^{-1}. (e) Average current density of anode and cathode scans at 0.05 V vs SCE as a linear function of scan rate for NP Au/Cr-NiFe, Au/NiFe, Au/NiCr and Au/FeCr hybrid electrodes. The linear slope is the double-layer capacitance, C_{dl}.

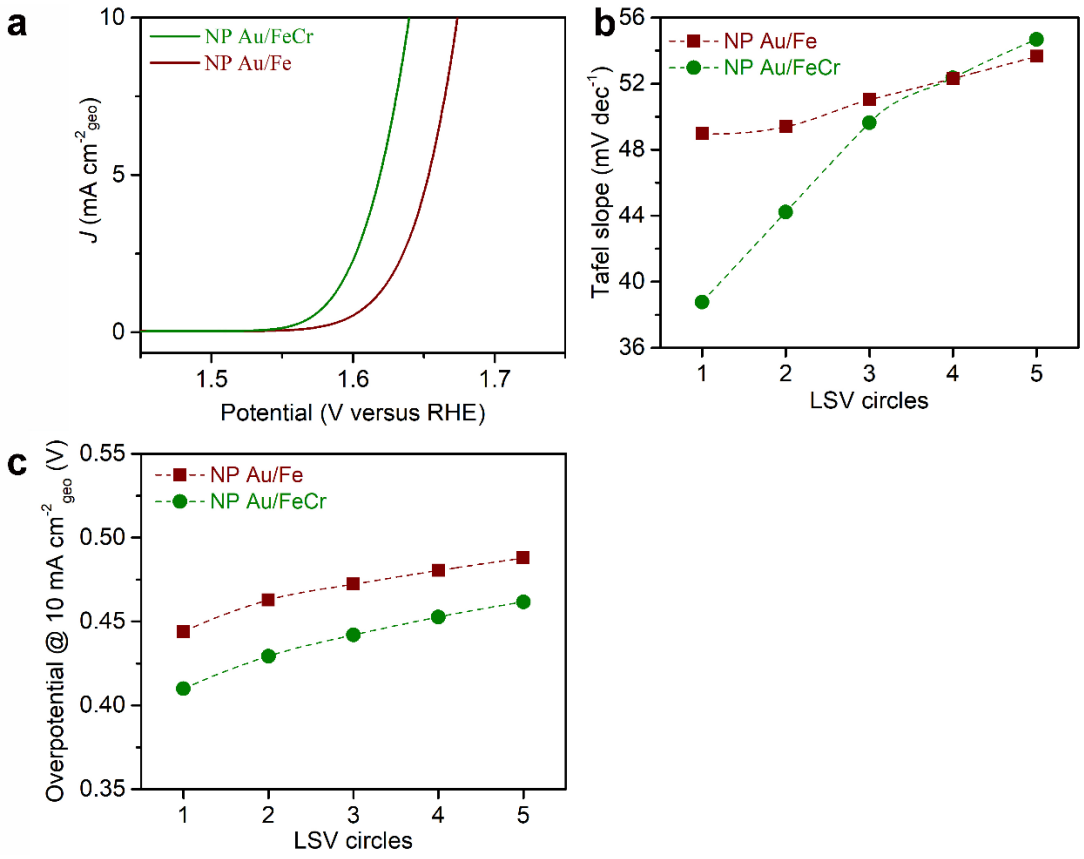

Fig. S15. (a) The 1st LSV curves for NP Au/Fe and NP Au/FeCr hybrid electrodes with the scan rate of 10 mV s^{-1} in 0.1 M KOH. LSV curves for NP Au/Fe and NP Au/FeCr hybrid electrodes start at the potential of 1.2616 V vs RHE and end up with the current density of 10 mA cm^{-2}_{geo}. (b) Tafel slopes of the first five LSV curves for NP Au/Fe and NP Au/FeCr hybrid electrodes. (c) Overpotentials at 10 mA cm^{-2}_{geo} of the first five LSV curves for NP Au/Fe and NP Au/FeCr hybrid electrodes.

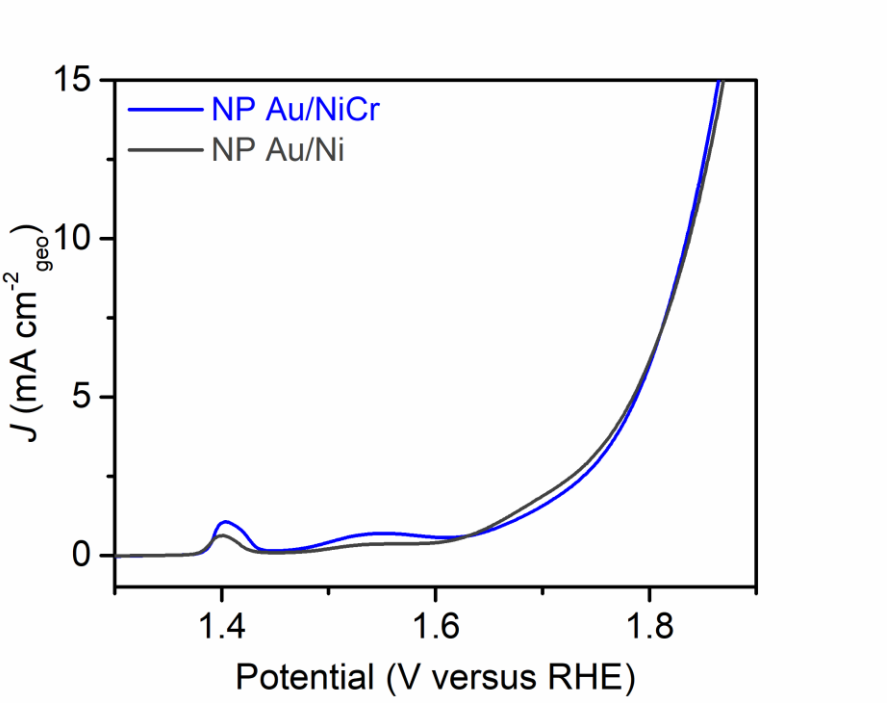

Fig. S16. The LSV curves for NP Au/Ni and NP Au/NiCr hybrid electrodes with the scan rate of 10 mV s^{-1} in 0.1 M KOH.

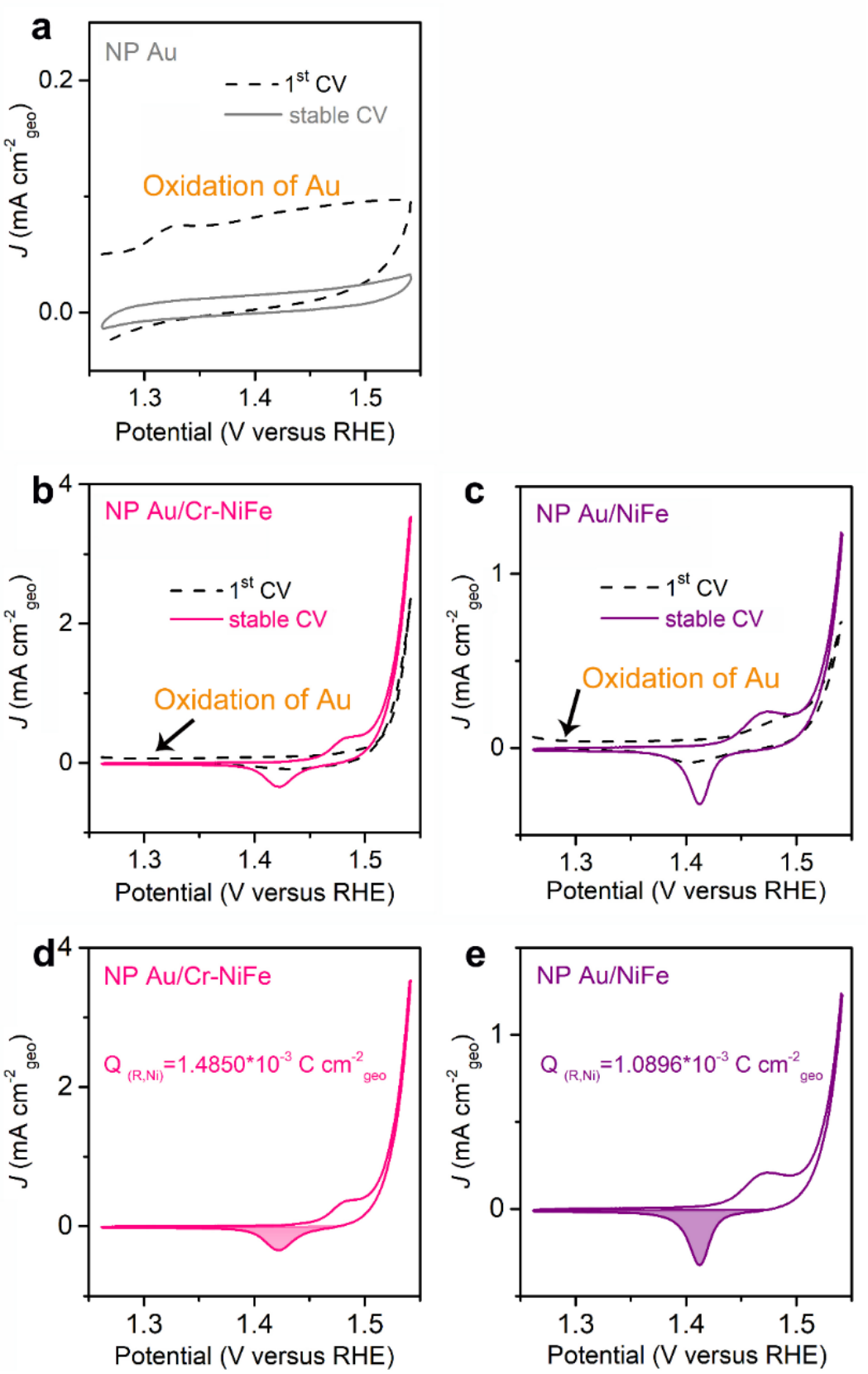

Fig. S17. Comparison of CV curves of the 1st cycle and the stable 15th cycle for (a) NP Au, (b) NP Au/Cr-NiFe and (c) NP Au/NiFe hybrid electrodes, respectively. Scan rate: 10 mV s^{-1}. In the potential range (1.26~1.4 V versus RHE) of the 1st circle CV, where

there are no Ni^{2+}/Ni^{3+} redox peaks from (oxy)hydroxides, oxidation currents of Au can be clearly identified for NP Au/Cr-NiFe and NP Au/NiFe hybrid electrodes, which indicates all oxyhydroxides deposited on Au ligaments can participate in OER. Typical CV curves of (d) NP Au/Cr-NiFe and (e) NP Au/NiFe hybrid electrodes, respectively. The corresponding Ni^{3+}/Ni^{2+} reduction peaks are shaded. $Q_{(R,Ni)}$ is the quantity of electric charge for Ni reduction peaks.

Due to the partial overlap between the Ni oxidation peaks current and the OER current, we use the Ni reduction peaks to calculate the quantity of electric charge involved in Ni redox reaction:

$$Q_{(R,Ni)} = \int Idt = \int Id\frac{U}{v} = \frac{S_{(R,Ni)}}{v} \tag{1}$$

where $Q_{(R,Ni)}$ is the quantity of electric charge (C) for Ni reduction peaks, I is current density (A cm^{-2}_{geo}) of Ni reduction peaks at some potential, U (V) is potential range of Ni reduction peaks, t stands for time (s), v is scan rate of CV (V s^{-1}), and $S_{(R,Ni)}$ is integral area of reduction peaks. All the computational process is based on one square centimeter. The TOF values of total metal sites (Ni, Fe and Cr) in potential-cycled NP Au/Cr-NiFe and NP Au/NiFe electrodes are calculated by the following formula:

$$TOF = \frac{J*A}{4*F*n} = \frac{J*A}{4*F*\frac{1}{x}*n_{(Ni)}} = \frac{x*J*A}{4*F*\frac{Q_{(R,Ni)}}{Q_e*NA}} = \frac{x*J*A}{4*Q_{(R,Ni)}} \tag{2}$$

where J is the OER current density (A cm^{-2}_{geo}) at some overpotential, A is the unit geometric area of the specimen, 4 stand for four-electron transfer when one O_2 forming, F is the Faraday constant, n and $n_{(Ni)}$ are the molar number of total metal sites (Ni, Fe and Cr) and Ni sites in potential-cycled hybrid electrodes including $Ni_xFe_yCr_{1-x-y}OOH$, NA is the Avogadro constant, and Q_e is the quantity of electric charge of one electron.

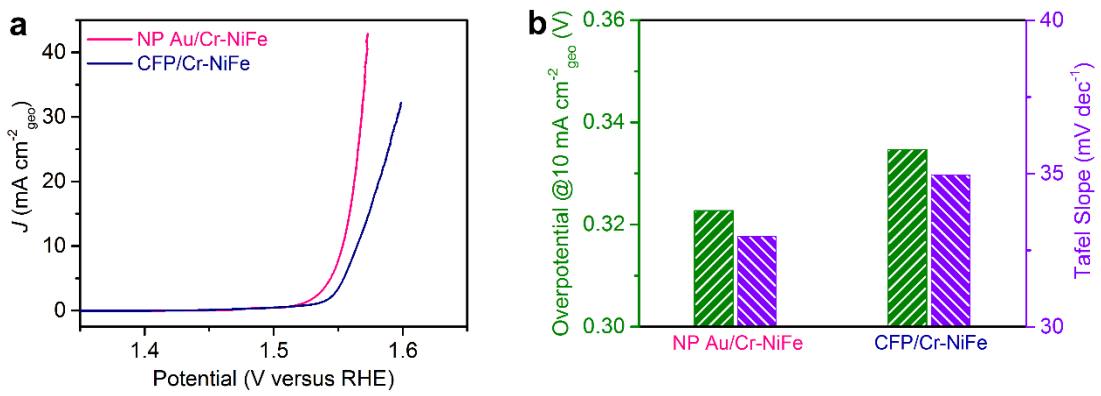

Fig. S18. (a) OER polarization curves in 0.1 M KOH solution for the Cr-doped NiFe oxyhydroxides supported by nanoporous Au and carbon fiber paper (CFP). (b) Comparison of Tafel slopes and overpotentials at the current density of 10 mA cm^{-2}_{geo} for NP Au/Cr-NiFe and CFP/Cr-NiFe.

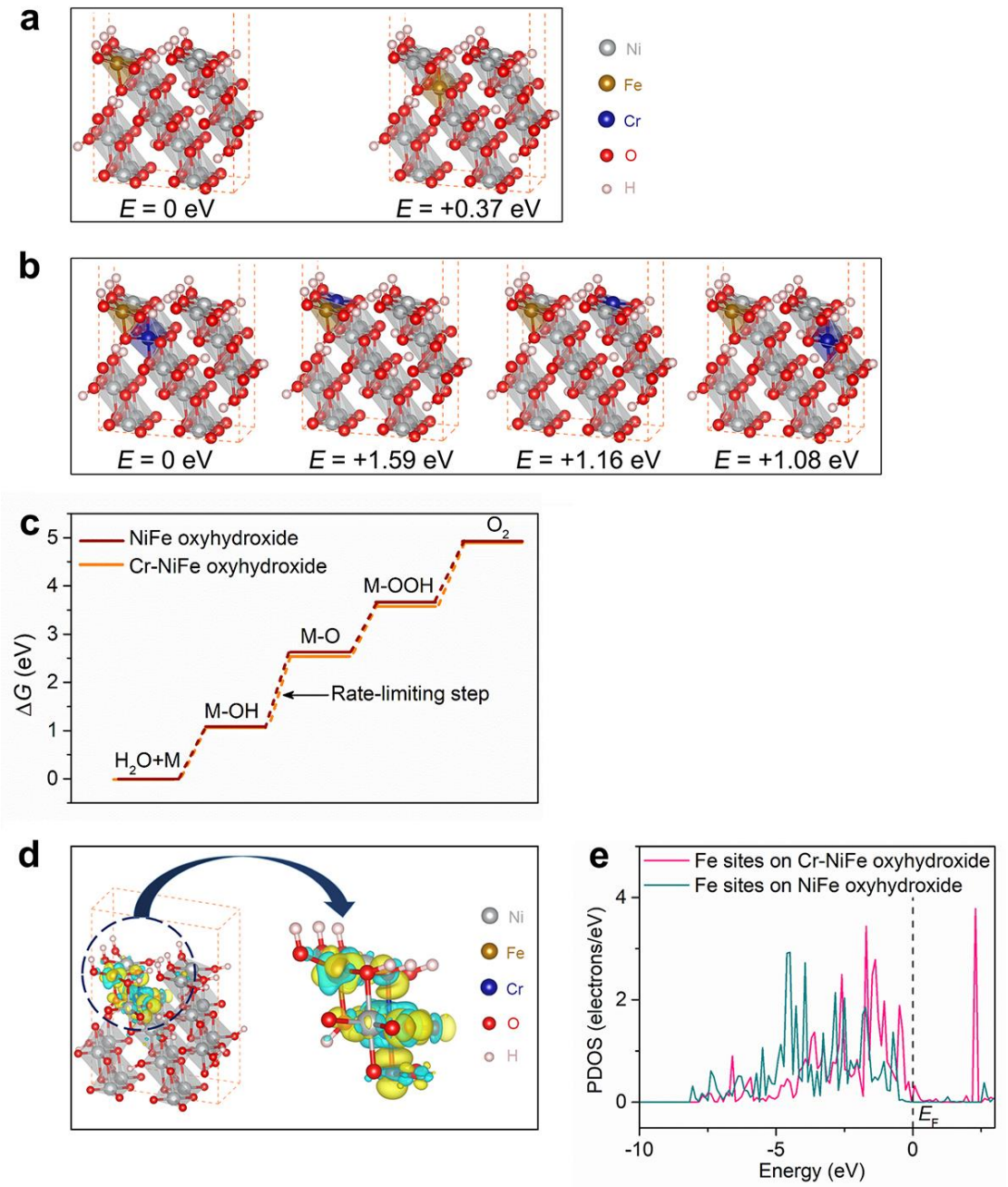

Fig. S19. DFT simulations to demonstrate the thermodynamic stability for (a) NiFe and (b) Cr-doped NiFe oxyhydroxides. (c) Gibbs free energy diagram for the four steps of OER on NiFe oxyhydroxide with and without Cr dopant. (d) Differential charge density of Cr-NiFe oxyhydroxide. Isosurface value is 0.005 eÅ^{-3}. Yellow and blue contours represent electron accumulation and depletion, respectively. (e) Projected densities of states (PDOS) for the edge Fe active sites in the Cr-doped NiFe oxyhydroxide and the pristine NiFe oxyhydroxide.

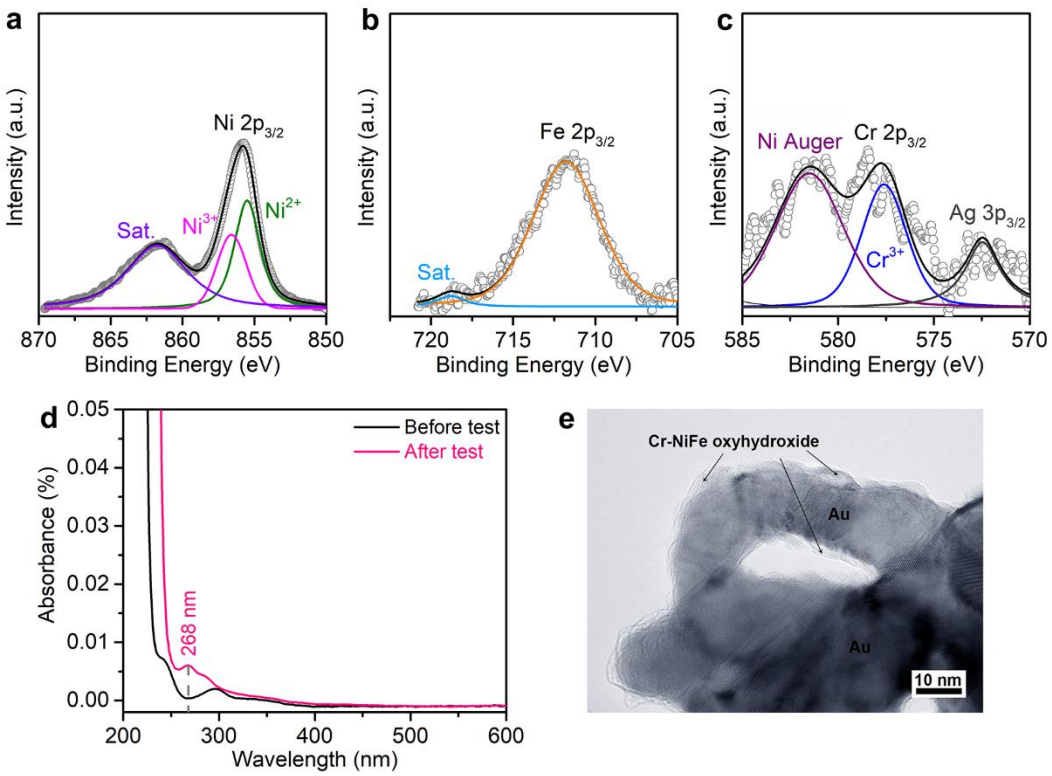

Fig. S20. High-resolution XPS spectra of (a) Ni $2p_{3/2}$, (b) Fe $2p_{3/2}$ and (c) Cr $2p_{3/2}$ for NP Au/Cr-NiFe oxyhydroxide hybrid electrode after the stability test. (d) UV-vis absorption spectra of 0.1 M KOH solution before and after stability test. Owing to the slight dissolution of NP Au/Cr-NiFe hybrid electrode, $Ni(OH)_3^-$ can be detected at the wavelength of 268 nm by UV-Visible spectrum. (e) Typical TEM image of NP Au/Cr-NiFe hybrid electrodes after stability measurement.

Table S1. Electrodeposition conditions for the fabrication of four NP Au/Cr-NiFe, NP Au/NiFe, NP Au/FeCr, NP Au/Fe, NP Au/NiCr and NP Au/Ni hybrid electrodes.

Specimens	**Electrolyte/mM**			
	$(NH_4)_2SO_4$	$NiSO_4$	$FeSO_4$	H_2CrO_4
NP Au/$Fe_{0.55}Cr_{0.45}$	3	0	0.25	0.45
NP Au/Fe	3	0	0.25	0
NP Au/Ni_1Cr_0	3	1	0	0.45
NP Au/Ni	3	1	0	0
NP Au/$Ni_{0.83}Fe_{0.17}$	3	1	0.5	0
NP Au/$Ni_{0.90}Fe_{0.10}Cr_0$	3	1	0.25	0
NP Au/$Ni_{0.81}Fe_{0.17}Cr_{0.02}$	3	1	0.25	0.45
NP Au/$Ni_{0.89}Fe_{0.10}Cr_{0.01}$	3	1	0.25	0.75

Table. S2. The onset overpotentials (η) of NP Au/Cr-NiFe hybrid electrodes in 0.1 M KOH and 1 M KOH electrolytes are compared with the current representative OER catalysts.

Samples	Electrolytes	Onset η (V)
NP Au/$Ni_{0.90}Fe_{0.10}Cr_0$	0.1 M KOH	0.270
NP Au/$Ni_{0.81}Fe_{0.17}Cr_{0.02}$	0.1 M KOH	0.256
NP Au/$Ni_{0.89}Fe_{0.10}Cr_{0.01}$	0.1 M KOH	0.256
NF/oLCFO-Ar [6]	0.1 M KOH	0.27
$CaCu_3Fe_4O_{12}$ [7]	0.1 M KOH	0.245
$LiNi_{0.8}Al_{0.2}O_2$ [9]	0.1 M KOH	0.30
BCFSn-721 [10]	0.1 M KOH	0.30
Cu@NCNT/Co_xO_y [11]	0.1 M KOH	0.27
nNiFe LDH/NGF [12]	0.1 M KOH	0.265
$Ni_{0.9}Fe_{0.1}$/NC [13]	0.1 M KOH	0.265
$SrNb_{0.1}Co_{0.7}Fe_{0.2}O_{3-\delta}$ [14]	0.1 M KOH	0.26
NiCd(A)Fe [15]	0.1 M NaOH	0.255
$MnFe_2O_4/NiCo_2O_4$ [16]	0.1 M KOH	0.28
NP Au/ $Ni_{0.81}Fe_{0.17}Cr_{0.02}$	1 M KOH	0.235
$Co_{0.46}Fe_{0.54}(OH)_2$ [17]	1 M KOH	0.245
$CoFe_2O_4$/PANI-MWCNT [18]	1 M KOH	0.265
Co-Fe NAFS [19]	1 M KOH	0.27
$Fe_3O_4@Co_9S_8$/rGO-2 [20]	1 M KOH	0.25
$NiFeO_x$/CFP [21]	1 M KOH	0.24
NiFe–MoO_x NS [22]	1 M KOH	0.235
$NiCeO_xAu$ [23]	1 M NaOH	0.215
NiFe/$NiCo_2O_4$ /NF [24]	1 M KOH	0.24
$Ni_3FeAl_{0.91}$–LDH/NF [25]	1 M KOH	0.26
$TaO_2F/^gC$ [26]	1 M KOH	0.25

References

1 S. Klaus, Y. Cai, M. W. Louie, L. Trotochaud, A. T. Bell, *J. Phys. Chem. C*, 2015, **119**, 7243−7254.

2 Y. Zhao, R. Nakamura, K. Kamiya, S. Nakanishi, K. Hashimoto, *Nat. Commun.*, 2013, **4**, 2390.

3 C. W. Tung, Y. Y. Hsu, Y. P. Shen, Y. Zheng, T. S. Chan, H. S. Sheu, Y. C. Cheng, H. M. Chen, *Nat. Commun.*, 2015, **6**, 8106.

4 S. Yagi, I. Yamada, H. Tsukasaki, A. Seno, M. Murakami, H. Fujii, H. Chen, N. Umezawa, H, Abe, N. Nishiyama, S. Mori, *Nat. Commun.*, 2015, **6**, 8249.

5 G. Chen, W. Zhou, D. Guan, J. Sunarso, Y. Zhu, X. Hu, W. Zhang, Z. Shao, *Sci. Adv.*, 2017, **3**, e1603206.

6 B. Q. Li, C. Tang, H. F. Wang, X. L. Zhu, Q. Zhang, *Sci. Adv.*, 2016, **2**, e1600495.

7 S. Yagi, I. Yamada, H. Tsukasaki, A. Seno, M. Murakami, H. Fujii, H. Chen, N. Umezawa, H, Abe, N. Nishiyama, S. Mori, *Nat. Commun.*, 2015, **6**, 8249.

8 Z. Lu, H. Wang, D. Kong, K.Yan, P. Hsu, G. Zheng, H. Yao, Z. Liang, X. Sun, Y. Cui, *Nat. Commun.*, 2014, **5**, 4345.

9 A. Gupta, W. D. Chemelewski, C. B. Mullins, J. B. Goodenough, *Adv. Mater.*, 2015, **27**, 6063–6067.

10 X. Xu, C. Su, W. Zhou, Y. Zhu, Y. Chen, Z. Shao, *Adv. Sci.*, 2016, **3**, 1500187.

11 X. Zhao, F. Li, R. Wang, J. Seo, H. Choi, S. Jung, J. Mahmood, I. Jeon, J. Baek, *Adv. Funct. Mater.*, 2017, **27**, 1605717.

12 C. Tang, H. Wang, H. Wang, Q. Zhang, G. Tian, J. Nie, F. Wei, *Adv. Mater.*, 2015, **27**, 4516–4522.

13 X. Zhang, H. Xu, X. Li, Y. Li, T. Yang, Y. Liang, *ACS Catal.*, 2016, **6**, 580−588.

14 Y. Zhu, W. Zhou, Z. Chen, Y. Chen, C. Su, M. O. Tadé, Z. Shao, *Angew. Chem. Int. Ed.,* 2015, **54**, 3897–3901.

15 J. Kim, D. H. Youn, K. Kawashima, J. Lin, H. Lim, C. B. Mullins, *Appl. Catal. B-Environ.*, 2018, **225**, 1–7.

16 Y. Zhang, M. Li, B. Hua, Y. Wang, Y. Sun, J. Luo, *Appl. Catal. B-Environ*., 2018, **236**, 413–419.

17 M. S. Burke, M. G. Kast, L. Trotochaud, A. M. Smith, S. W. Boettcher, *J. Am. Chem. Soc.*, 2015, **137**, 3638−3648.

18 Y. Liu, J. Li, F. Li, W. Li, H. Yang, X. Zhang, Y. Liu, J. Ma, *J. Mater. Chem. A*, 2016, **4**, 4472–4478.

19 J. Nai, B. Y. Guan, L. Yu, X. W. Lou, *Sci. Adv.*, 2017, **3,** e1700732.

20 J. Yang, G. Zhu, Y. Liu, J. Xia, Z. Ji, X. Shen, S. Wu, *Adv. Funct. Mater.*, 2016, **26**, 4712–4721.

21 H. Wang, H. Lee, Y. Deng, Z. Lu, P. Hsu, Y. Liu, D. Lin, Y. Cui, *Nat. Commun.*, 2015, **6**, 7261.

22 C. Xie, Y. Wang, K. Hu, L. Tao, X. Huang, J. Huo, S. Wang, *J. Mater. Chem. A*, 2017, **5**, 87–91.

23 J. W. D. Ng, M. García-Melchor, M. Bajdich, P. Chakthranont, C. Kirk, A. Vojvodic, T. F. Jaramillo, *Nat. Energy.*, 2016, **1**, 16053.

24 C. Xiao, Y. Li, X. Lu, C. Zhao, *Adv. Funct. Mater.*, 2016, **26**, 3515–3523.

25 H. Liu, Y. Wang, X. Lu, Y. Hu, G. Zhu, R. Chen, L. Ma, H. Zhu, Z. Tie, J. Liu, Z. Jin, *Nano Energy*, 2017, **35**, 350–357.

26 X. Yue, Y. Jin, P. K. Shen, *J. Mater. Chem. A*, 2017, **5**, 8287−8291.